The Astrophysical Journal, 934:8 (16pp), 2022 July 20 https://doi.org/10.3847/1538-4357/ac7643

The Mysterious Affair of the H_2 in AU Mic

Laura Flagg[1,2], Christopher M. Johns-Krull[1], Kevin France[3], Gregory Herczeg[4], Joan Najita[5], Allison Youngblood[3], Adolfo Carvalho[6], John Carptenter[7], Scott J. Kenyon[8], Elisabeth Newton[9], and Keighley Rockcliffe[9]
[1] Department of Physics and Astronomy, Rice University, 6100 Main Street, MS-108, Houston, TX 77005, USA; laura.flagg@cornell.edu
[2] Department of Astronomy and Carl Sagan Institute, Cornell University, Ithaca, New York 14853, USA
[3] Laboratory for Atmospheric and Space Physics, University of Colorado, 600 UCB, Boulder, CO 80309, USA
[4] Kavli Institute for Astronomy and Astrophysics, Peking University, Yi He Yuan Lu 5, Haidian Qu, Beijing 100871, People's Republic of China
[5] NOIRLab, 950 Cherry Avenue, Tucson, AZ, 85719, USA
[6] Cahill Center for Astronomy & Astrophysics, California Institute of Technology, Pasadena, CA 91125, USA
[7] Joint ALMA Observatory, Avenida Alonso de Ćordova 3170, Santiago, Chile
[8] Smithsonian Astrophysical Observatory, 60 Garden Street, Cambridge, MA 02138 USA
[9] Department of Physics and Astronomy, Dartmouth College, Hanover, NH 03755, USA
Received 2021 November 17; revised 2022 June 1; accepted 2022 June 2; published 2022 July 20

Abstract

Molecular hydrogen is the most abundant molecule in the galaxy and plays important roles in planets, their circumstellar environments, and many of their host stars. We have confirmed the presence of molecular hydrogen in the AU Mic system using high-resolution FUV spectra from HST-STIS during both quiescence and a flare. AU Mic is a ∼23 Myr M dwarf that hosts a debris disk and at least two planets. We estimate the temperature of the gas at 1000–2000 K, consistent with previous detections. Based on the radial velocities and widths of the H_2 line profiles and the response of the H_2 lines to a stellar flare, the H_2 line emission is likely produced in the star, rather than in the disk or the planet. However, the temperature of this gas is significantly below the temperature of the photosphere (∼3650 K) and the predicted temperature of its starspots ($\gtrsim$2650 K). We discuss the possibility of colder starspots or a cold layer in the photosphere of a pre-main-sequence M dwarf.

Unified Astronomy Thesaurus concepts: Exoplanet formation (492); Debris disks (363); Low mass stars (2050); Starspots (1572); Circumstellar gas (238); High resolution spectroscopy (2096); Exoplanets (498); Pre-main sequence stars (1290); Stellar atmospheres (1584)

1. Introduction

Planetary systems undergo dramatic changes for the first ∼100 Myr after their formation. How a given planet evolves is a direct function of how both the host star and any circumstellar disk evolve and how they affect each other. In order to study such complex interactions, observations of systems with circumstellar disks and planets are needed.

One important issue is the state of the gas in the inner disk. Because gas, especially warm gas, is hard to detect unless there are large amounts present, much less is known about the evolution of gas in the inner disk once gas stops accreting onto the star (e.g., Hughes et al. 2018). Observationally, it has been hard to distinguish between a reduction of the mass of gas and the complete absence of gas (Flagg et al. 2021). Traditionally, it has been thought that the gas has completely dissipated once accretion is no longer detectable, but recent observations of systems like TWA 4 (Yang et al. 2012) or TWA 7 (Flagg et al. 2021) show that this is not always true.

One potential avenue to search for small amounts of H_2 is far-UV observations (Ingleby et al. 2009; Alcalá et al. 2019). Molecular hydrogen—which is the dominant component of protoplanetary disks—only has allowed transitions in the UV. The FUV (∼1000–2000 Å) is particularly sensitive to warm gas (see Section 5), such as the gas that could still be present in the inner regions of developing solar systems. However, with limited spatial resolution, it can be difficult if not impossible to distinguish small amounts of circumstellar H_2 from the H_2 that exists in stars. M dwarfs exhibit H_2 emission, possibly from their photospheres (Kruczek et al. 2017); warmer stars, like the Sun, have H_2 in starspots (Jordan et al. 1978), which are similar in temperature to the photospheres of M dwarfs.

A way around this problem is to observe systems with well-known inclinations that are not face on. In these systems, if the signal-to-noise ratio of the spectrum is high enough to trace the H_2 line profile, the shape of the profile can help indicate the origin of the H_2 (Kruczek et al. 2017). If, for example, the line profile is much broader than typical line profiles for the star, then the H_2 probably originates in a circumstellar disk, orbiting the star at high velocities. However, the opposite is not necessarily true, as circumstellar gas farther out may produce a narrow profile.

Based on these criteria, an obvious target for the study of H_2 is AU Mic. AU Mic is a M0Ve star (Pecaut & Mamajek 2013; see Table 1 for additional properties) that is part of the ∼23 Myr β Pic Moving Group (Barrado y Navascués et al. 1999; Mamajek & Bell 2014; Shkolnik et al. 2017). It has an edge-on debris disk discovered by Kalas et al. (2004). The dust in the debris disk has since been observed and imaged in the optical, NIR, FIR, and submillimeter/millimeter (e.g., Krist et al. 2005; Graham et al. 2007; Wilner et al. 2012; MacGregor et al. 2013; Matthews et al. 2015; Wang et al. 2015).

However, these are all observations of the dust content of the disk. The characteristics of any gas in the disk remain uncertain. Planet formation is greatly influenced by the gas, and not just because gas is an important component of planets themselves. Gas influences the motion of the small dust grains in the disk via gas drag (e.g., Weidenschilling 1977;

Table 1
Parameters of the AU Mic System

Parameter	Value	Citation
SpT	M0Ve	Pecaut & Mamajek (2013)
RV (km s^{-1})	-4.25 ± 0.24	Schneider et al. (2019)
v sin i (km s^{-1})	8.7 ± 2.0	Plavchan et al. (2020)
M_* ($M_\odot$)	0.50 ± 0.03	Plavchan et al. (2020)
Age (Myr)	~23 Myr	Mamajek & Bell (2014)
$T_{\rm eff}$ (K)	3642 ± 22	Pecaut & Mamajek (2013)

Youdin & Goodman 2005), induces spirals and rings (Lyra & Kuchner 2013), and can alter planet orbits (e.g., Goldreich & Sari 2003; Baruteau et al. 2014). The presence of warm gas in a disk may also explain the discrepancy between the terrestrial planet population and the lack of detected IR flux from giant impacts that should be associated with the formation of these planets, because gas in the planet-forming region can "sweep away" dust (Kenyon et al. 2016), as models indicate that terrestrial planet formation during that stage should produce detectable IR excess.

Unfortunately, circumstellar gas around AU Mic has been hard to detect and characterize. Liu et al. (2004) searched for—but failed to find—CO $J = 3$–2 in its disk using the SCUBA bolometer array. Roberge et al. (2005) placed upper limits on the H_2 in the disk using FUV observations from FUSE ($R \sim 20{,}000$; 905–1187 Å) and STIS ($R \sim 46{,}000$; 1144 to 1710 Å). France et al. (2007) detected H_2 from the system during quiescence and concluded that due to its relatively low temperature between 800 and 2000 K, H_2 is in the disk, not the star. Kruczek et al. (2017) also detected H_2 during quiescence. Further upper limits on the amount of atomic of H, He, and C were obtained from X-ray observations by Schneider & Schmitt (2010). Daley et al. (2019) calculated an upper limit of 1.7×10^{-7} to $8.7 \times 10^{-7} M_\oplus$ of cold CO with excitation temperatures between 10 and 250 K based on ALMA data. Overall, the gas content has been elusive to quantify or characterize. Based on current measurements, the amount of gas in AU Mic's disk is clearly quite low, and there is a possibility that the H_2 detected does not lie in the disk (Kruczek et al. 2017).

Even prior to the discovery of AU Mic's disk, the star was well known for its flares, which were first detected in the optical by Kunkel (1970); since then, the flares have been studied in the EUV, X-ray, and radio (e.g., Monsignori Fossi et al. 1996; Smith et al. 2005; MacGregor et al. 2020). Recently, two young Neptunes, AU Mic b and c, have been discovered in transit around the star, at distances of 0.06 and 0.11 au, respectively (Plavchan et al. 2020; Martioli et al. 2021). Due to its relative proximity, the star and disk are comparatively well studied, making AU Mic a prototype for young M-dwarf planetary systems. Understanding its inner disk gas content would provide constraints on the gas available for the planets to accrete and help us understand what is driving the dynamics at this point in the system's evolution.

2. Observations

We used HST-STIS FUV-MAMA spectra of AU Mic from August 1998 (Pagano et al. 2000) and July 2020 taken with the E140M grating with the 0.″2 X 0.″2 aperture in timetag mode. The spectra cover 1144–1710 Å with resolving power $R \sim 46{,}000$ depending on the grating order. The observations are summarized in Table 2. AU Mic was observed for a total of 10105.74 s in 1998 (PID: 7556; PI: J. Linsky) and 15463.073 s in 2020 (PID: 15836; PI: E. Newton). Due to the decreasing sensitivity of the instrument with time, based on Carlberg & Monroe (2017), we extrapolate that by 2020 the instrument had between 70% and 85% of the sensitivity it had in 1998, depending on the order.

Table 2
Observation of AU Mic Taken with HST-STIS Using the E140M Grating with the 0.″2 X 0.″2 Aperture

Data set	Exp Time (s)	ID	MJD mid (days)
O4Z301010	2130.180	7556	51062.52430
O4Z301020	2660.189	7556	51062.58529
O4Z301030	2660.189	7556	51062.65248
O4Z301040	2655.182	7556	51062.71963
OE4H01010	2306.173	15836	59032.03795
OE4H01020	2848.183	15836	59032.10325
OE4H02010	2306.188	15836	59032.24029
OE4H02020	2848.192	15836	59032.30198
OE4H02030	2848.169	15836	59032.36822
OE4H03010	2306.168	15836	59033.03164

Note. The horizontal line divides the data taken in August 1998 (top) from the data taken in July 2020 (bottom).

The spectra were reduced with the STIS pipeline.[10] We then interpolated each observation onto a common wavelength scale. We then did an initial analysis of the observations from each HST orbit separately. During the 2020 observations, there was a significant flare during the first exposure (Figure 1), and two of the later exposures were taken during a transit of AU Mic b. We therefore analyzed those exposures separately; the other three exposures were coadded for further analysis. There was also a more minor flare during the first exposure of the 1998 data, analyzed by Robinson et al. (2001), and smaller flares that were still noticeable by eye during the second exposure. We coadded only the data from the two remaining exposure in 1998 for the analysis of the temperature (Section 5) as the temperature would be specially sensitive to the flare; all the data from 1998 were coadded for the purpose of analyzing the line profile, as presented in Sections 6.2.1 and 6.4.

3. H_2 Detection and Verification in Quiescence

We used the FUV spectra to detect H_2 during quiescence. The spectra are dominated by chromospheric lines, such as the ones noted in Figure 1. During quiescence, the individual H_2 features are buried in the continuum noise and are not bright enough to be detected on their own. Instead, we used two methods to combine the signals from multiple features: least-squares deconvolution (LSD), as implemented by Chen & Johns-Krull (2013), and a cross-correlation function (CCF). LSD is a way of extracting the average shape of the line profile from many lines across a spectrum (Donati et al. 1997). Both methods require a selection of H_2 lines (Abgrall et al. 1993) and their expected line strengths, for which we used models from McJunkin et al. (2016). We also set a minimum peak line intensity for each method to maximize the signal-to-noise ratio of our result. Using too many weak lines in both the CCF and

[10] https://github.com/spacetelescope/stistools

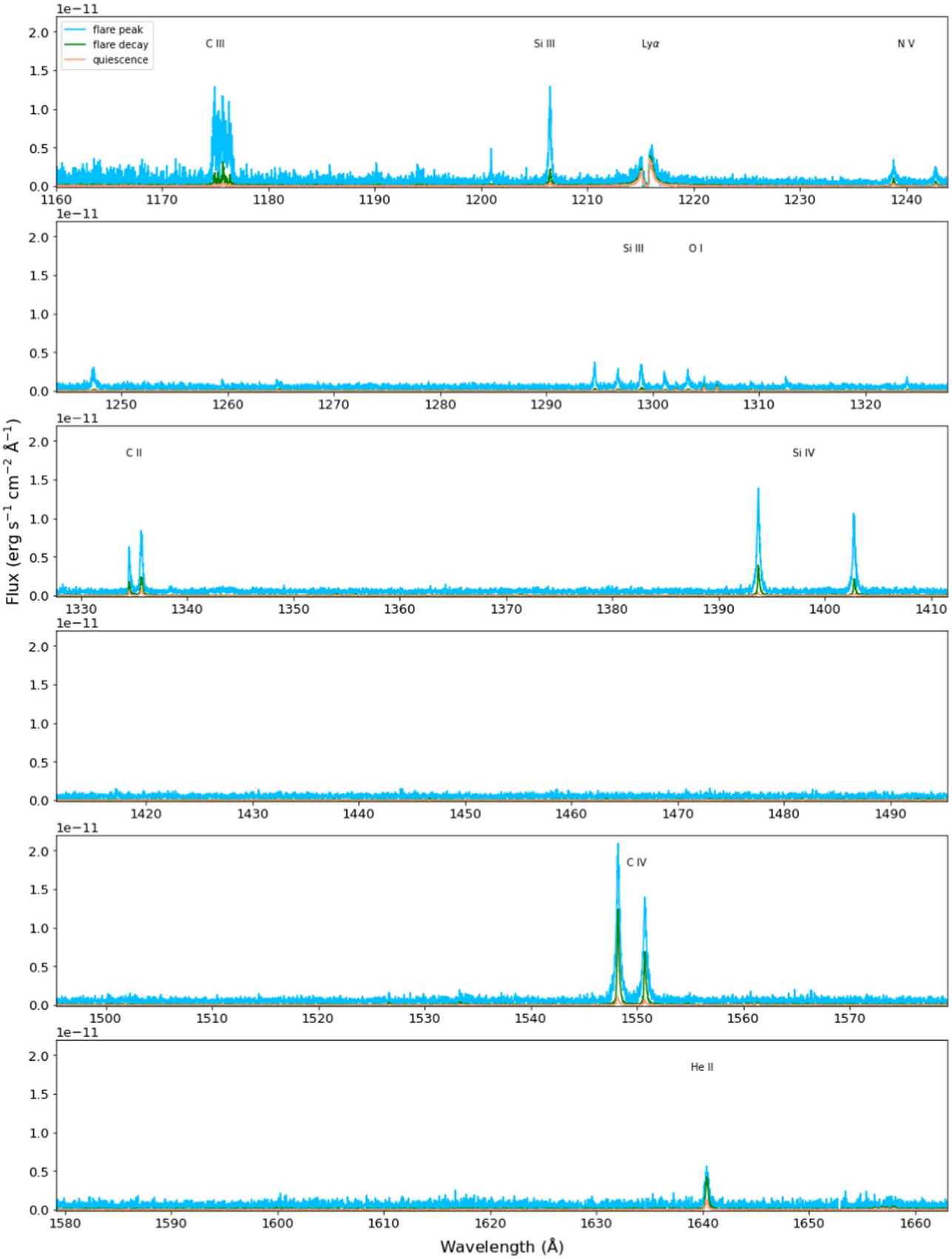

Figure 1. The spectra from 2020: in quiescence compared to while flaring. The features that change most visibly are hot chromospheric lines like Si IV or C IV.

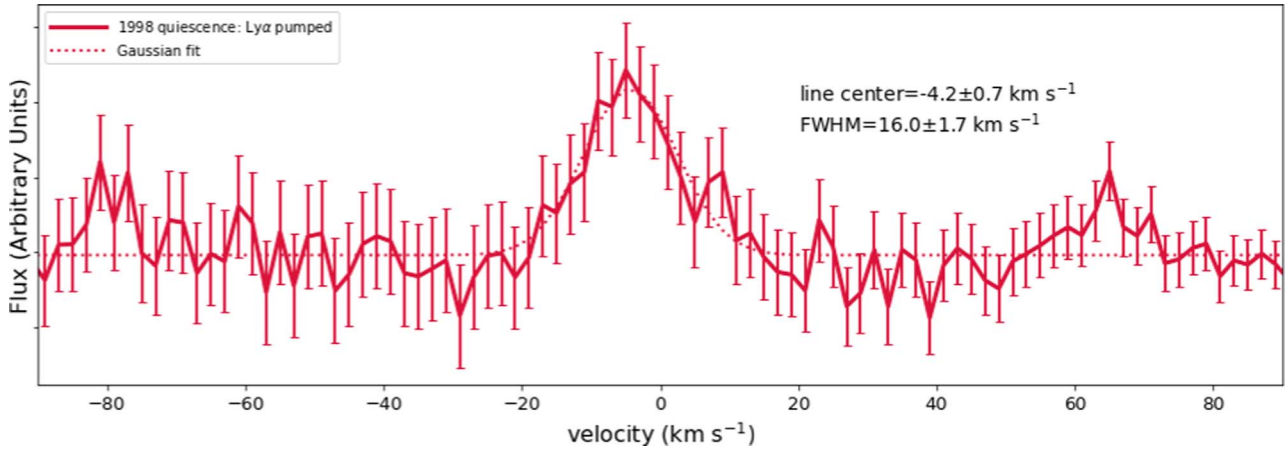

Figure 2. The line profile reconstructed using the LSD fit with a Gaussian. The line center is consistent with the systemic velocity of the star.

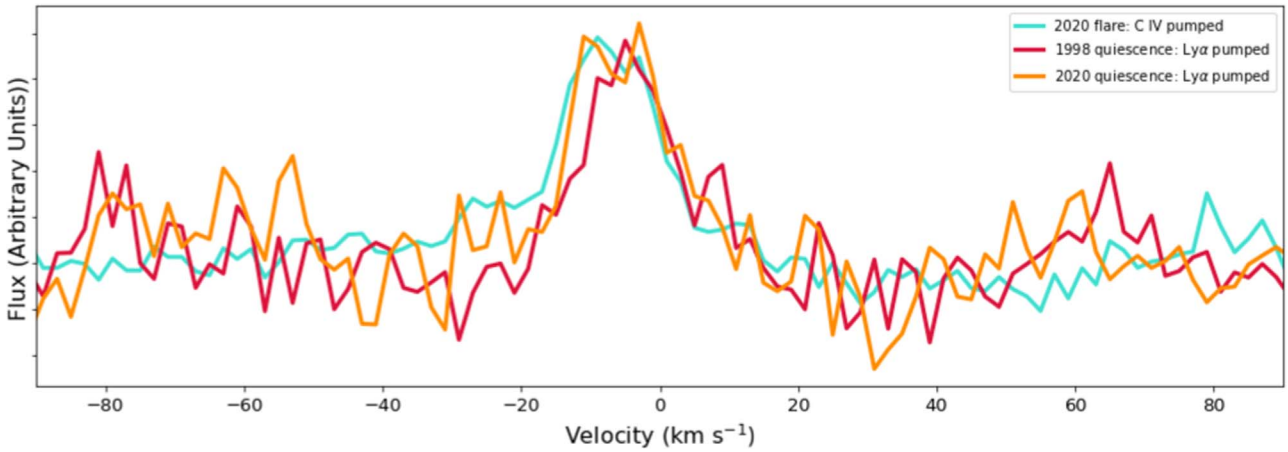

Figure 3. Comparison between the reconstructed line profiles for 1998 during quiescence, 2020 during quiescence, and 2020 during the flare. Note: the profiles are scaled to similar heights.

the LSD will increase the noise more than the signal. The specific minimum peak line intensity depends both on the method and the set of H_2 lines. LSD profiles and CCFs are sensitive to noise in different manners, so we chose a slightly different minimum peak line intensity based on what was appropriate for each method. We also looked at individual progressions, which are H_2 emission lines from the same excited state [v',J'],[11] thus changing the set of H_2 lines.

For the LSD (unlike the CCF described below), we are able to extract line profiles and associated uncertainties directly, using a minimum peak line intensity of 1×10^{-16} erg s^{-1} cm^{-2} Å^{-1}, resulting in one LSD profile combining all progressions for the 1998 data and another profile for the 2020 data. We can then do a basic analysis of these profiles by fitting Gaussians to them, as shown in Figure 2 for the data from 1998. The standard errors on the Gaussian fit are calculated from the covariance matrix. The line center from the LSD profile, -4.2 ± 0.7 km s^{-1}, is consistent within uncertainties with the systemic velocity of AU Mic of -4.25 ± 0.24 km s^{-1} (Schneider et al. 2019). The FWHM of the line is 16.0 ± 1.7 km s^{-1}. Figure 3 shows the resulting LSD profiles from 2020 compared to those from 1998. We see relatively similar profiles for the 1998 and 2020 data, as well as the 2020 flare, although the line profile from the 2020 data is slightly blueshifted. The Gaussian fits to all three profiles are summarized in Table 3.

Table 3
Fit Parameters and Uncertainties for All Three Profiles

Profile	Center (km s^{-1})	FWHM (km s^{-1})
1998 Quiescence	-4.2 ± 0.7	16.0 ± 1.7
2020 Quiescence	-5.7 ± 0.8	16.6 ± 1.9
2020 Flare	-7.7 ± 0.5	19.0 ± 1.2

Our procedure for creating the CCF of AU Mic is based on Flagg et al. (2021). To summarize, we masked out the hot gas lines from the star and then cross-correlated the masked stellar spectrum with H_2 templates. For this analysis, we used what Flagg et al. refers to as a segmented spectrum, a spectrum with only segments that contain H_2 features that are expected to be prominent. The segmented spectrum preserves the relative line heights of different H_2 features, which are needed to measure a temperature (see Section 5). In the data from 1998 to 2020, we clearly detect four progressions pumped by Lyα: [1,4] — detected previously by Kruczek et al. (2017)—as well as [1,7], [0,1], and [0,2], as shown in Figure 4.

[11] We use the notation [v',J'] to describe a progression, where v' and J' are the vibrational and rotational levels, respectively, in the first excited electronic state for a given progression.

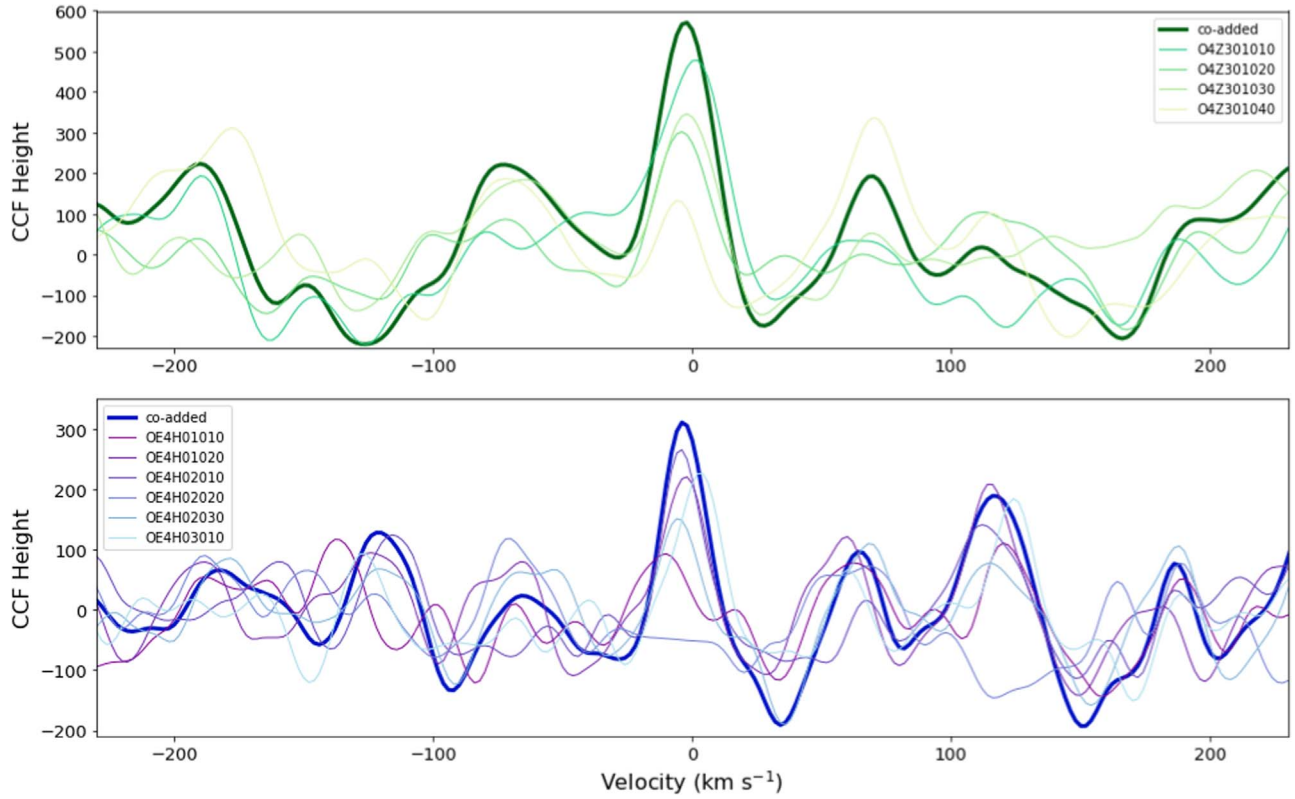

Figure 4. The CCFs from 1998 (top) and 2020 (bottom) both show a clear detection of H_2 from Lyα-pumped progressions. The thin lines are each separate orbit, with labels that correspond to the individual observations listed in Table 2. The thick lines are the CCF from the coadded spectrum.

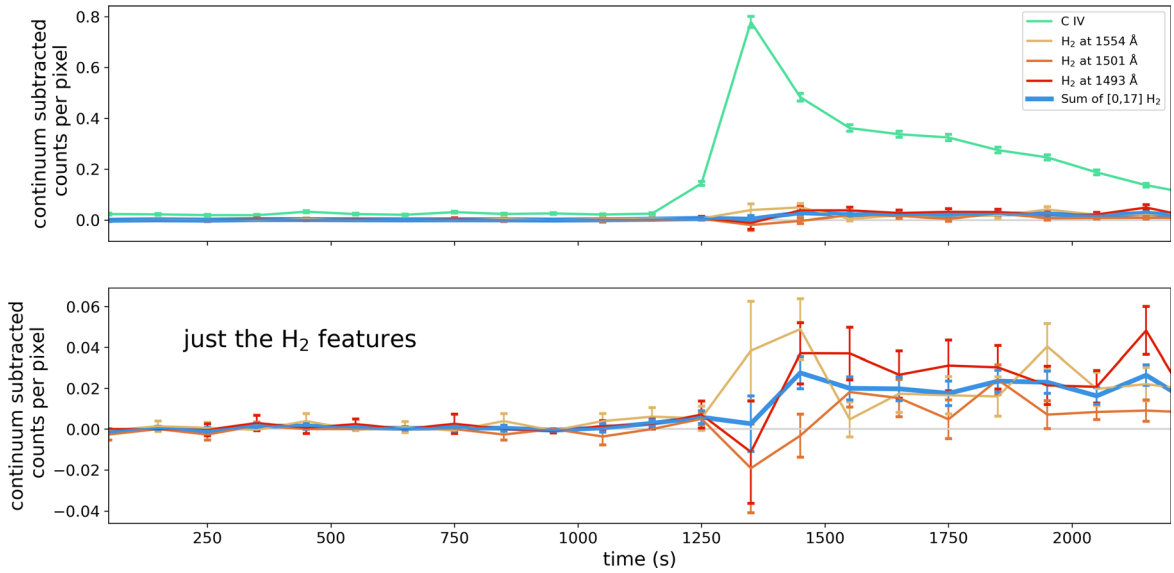

Figure 5. Continuum-subtracted light curves for different spectral features for observation OE4H01010 acquired on 2020 July 2. C IV (light-green line, top plot), which is a hot transition region line, peaks at 1350 s. The various H_2 features (shown more clearly in the bottom plot), are all in the [0,17] progression and pumped by C IV. The individual features have all clearly flared by 1550 s at the latest, with one feature flaring as early as 1350 s, and their combined brightness flaring by 1450 s, implying at most a 200 s delay between the C IV increasing in brightness and the resulting increase in brightness from H_2.

4. H_2 Detection during a Stellar Flare

The response of the H_2 emission during a stellar flare gives insight into the nature and source of the H_2. For both 1998 and 2020, the first exposure contains a stellar flare. In 1998, the flare (analyzed in detail by Robinson et al. 2001) was fairly weak, with flux from hot chromospheric lines like C IV increasing by less than a factor of 2. In comparison, the 2020 flare data in observation OE4H01010 was much stronger, with fluxes in chromospheric lines increasing by a factor of ~40, as shown in Figure 5. During both flares, we detect H_2 emission in the spectrum that is not detectable during quiescence. As the 2020 flare was significantly brighter than the 1998 flare, the H_2 was correspondingly brighter, so we focused our analysis on the 2020 data set. We show the spectra of two prominent H_2 features that flared in the 2020 data, both during the flare and in quiescence, in Figure 6.

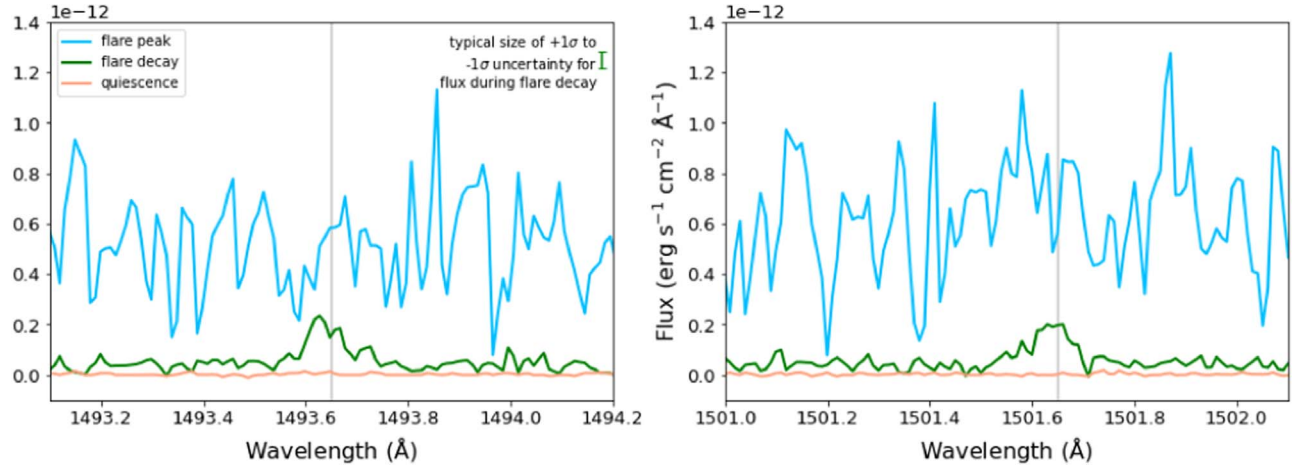

Figure 6. Spectra from 2020. The observation during the flare decay (green line) shows emission from H_2 features not seen during quiescence (orange line). During the flare peak, the noise in the continuum makes detecting any H_2 difficult.

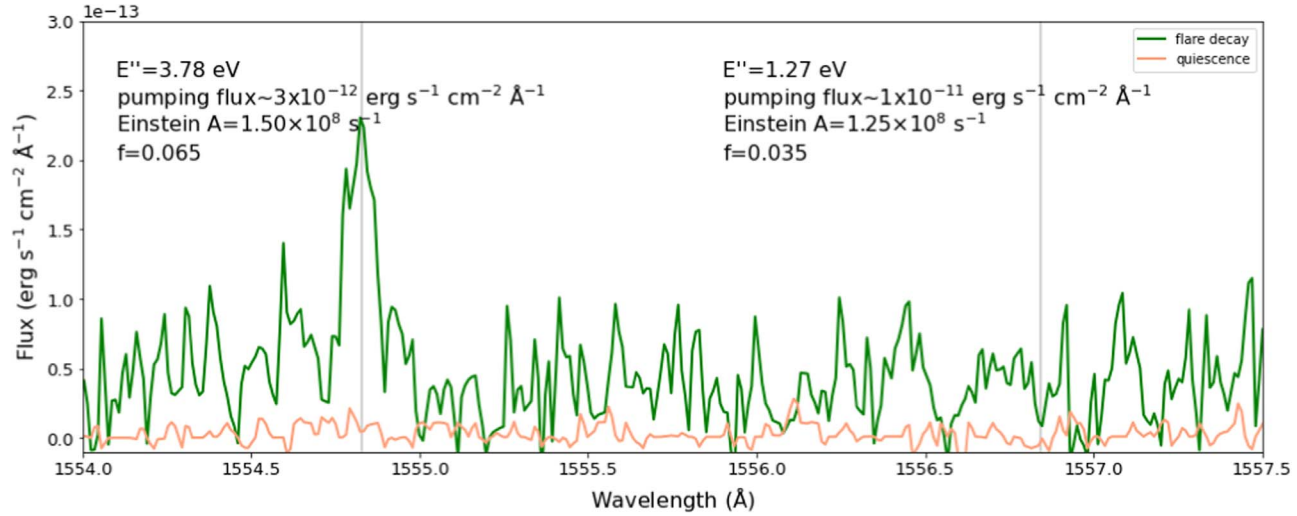

Figure 7. Two prominent H_2 features from [0,17] at 1554.8 Å and [1,7] at 1556.9 Å marked by vertical gray lines. During the flare decay (green line, observation OE4H01010 acquired on 2020 July 2), only the one that originates from a much higher energy level is detectable by eye, implying the H_2 level populations are affected by a nonthermal mechanism during the flare.

The H_2 features detectable by eye during the 2020 flare are from the [0,17] or the [0,24] progressions. (The spectra from all features are shown in the Appendix.) They are pumped by the C IV doublet at 1550 Å, whose brightness increased by ∼40× during the flare (Figure 1). The detection of the resulting H_2 lines is surprising, although not unprecedented (Herczeg et al. 2006), because these H_2 lines originate from states with energies of 3.78 and 4.19 eV above ground, compared to between 1.0 and 1.3 eV for lines in progressions we detect during quiescence. For example, during the flare, the H_2 feature at 1554.8 Å is quite strong, while the H_2 feature at 1556.9 Å is not (Figure 7). In thermal equilibrium at temperatures below 10,000 K, these flux ratios are not possible, because the line at 1556.9 Å is populated from a state with energy of 1.27 eV from the [1,7] progression while the line at 1554.8 Å is from the [0,17] progression populated from a state at 3.78 eV. Clearly, the flare results in nonthermal populations of H_2.

Overall, we detect flux from eight features from [0,17] and two features from [0,24], which are summarized in Table 4. These were the only H_2 progressions that clearly had extra emission during the flare. The flux from Lyα did not increase substantially during the flare (Figure 1), consistent with the findings from Loyd et al. (2018), and thus the H_2 lines that are pumped by Lyα show no significant increase in flux.

5. Temperature of H_2 in Quiescence

The temperature of the H_2 emission helps to constrain its origin. We estimate the gas temperature by analyzing the H_2 emission, assuming the gas is thermally populated while in quiescence. However, we cannot derive a gas temperature directly from H_2. Whether or not we detect flux from a progression and how much flux we see depends on several factors:

1. a populated lower state of the pumping transition of H_2 molecules,
2. a pumping transition with a relatively high oscillator strength,
3. flux to excite the H_2 molecule into higher states,
4. the Einstein A values of the decaying transitions for a progression, and
5. the filling factor of the gas.

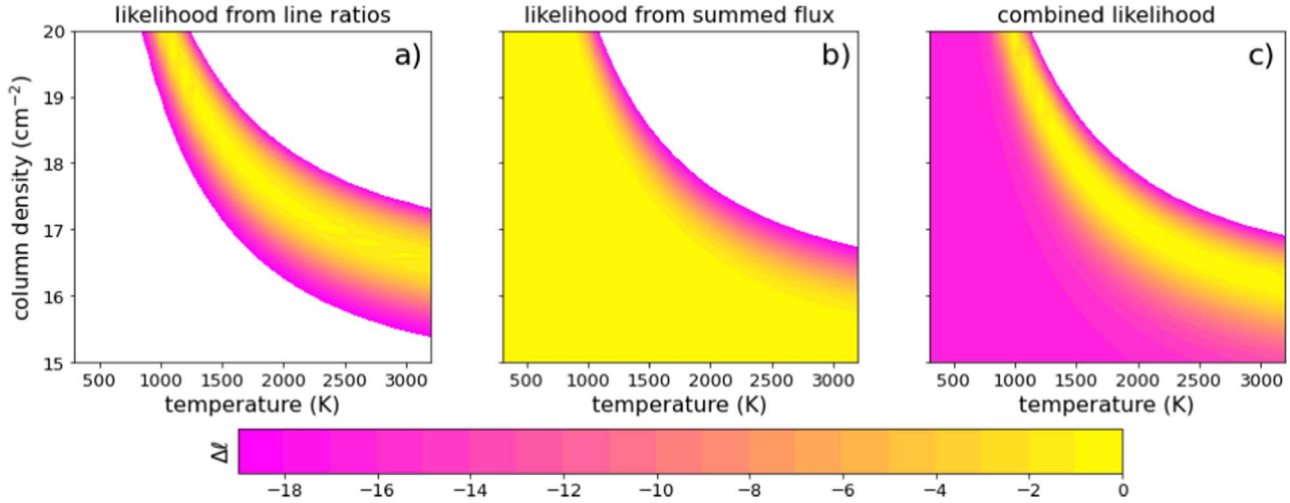

Figure 8. Log likelihoods for the temperature and H_2 column density of the gas.

Table 4
C IV-pumped H_2 Detections during Flare

Wavelength (Å)	Progression	Lower E (eV)	Flux $\times 10^{-15}$ (erg s^{-1} cm^{-2})	Einstein A (s^{-1})	Velocity (km s^{-1})	FWHM (km s^{-1})
1501.67	[0,17]	3.78	16.1 ± 2.8	21.78	−7.6	18.6
1493.67	[0,17]	3.78	17.1 ± 4.7	21.07	−7.1	13.1
1446.72	[0,17]	3.78	14.6 ± 3.6	19.48	−9.1	17.1
1554.85	[0,17]	3.78	20.1 ± 7.1	14.97	−6.1	14.1
1437.78	[0,17]	3.78	11.7 ± 2.8	14.35	−9.3	17.8
1391.01	[0,17]	3.78	7.8 ± 2.0	11.32	−8.4	12.8
1599.93	[0,17]	3.78	20.2 ± 10.6	9.59	−4.9	11.2
1381.41	[0,17]	3.78	3.3 ± 2.5	6.10	−5.2	14.4
1594.05	[0,24]	4.19	4.2 ± 3.6	23.06	−8.8	7.3
1586.69	[0,24]	4.19	7.7 ± 4.5	21.54	−4.0	17.2

Note. The listed velocity is relative to the listed wavelengths, which may be inaccurate by a few km s^{-1}.

Items (2) and (4) are solely dependent on molecular physics and therefore are well known. Item (3) depends on our knowledge of the flux at the pumping wavelength. In the case of H_2 lines pumped by hot chromospheric lines, this is typically trivial because we directly observe those pumping lines. However, the Lyα line profile is contaminated by ISM absorption, so for transitions pumped by Lyα, we need to reconstruct the Lyα line profile in order to estimate this flux. This was carried out for AU Mic following the methods of Youngblood et al. (2021). We derive a profile with an intrinsic integrated flux of 8.94×10^{-12} erg s^{-1} cm^{-2}, in agreement with the value reported in Youngblood et al. (2016). The difference between the two reconstructions is the approximation of the intrinsic emission line by a Voigt profile, which matches the broad wings better than the double-Gaussian approach of Youngblood et al. (2016). Item (5) is unknown, but is often assumed to be 1 (McJunkin et al. 2016). This leaves only item (1). If the H_2 lines are optically thin, which is the case for the low levels of emission we detect from AU Mic, and the H_2 is thermally populated in quiescence—which is consistent with models (Ádámkovics et al. 2016)—then the relative fluxes of H_2 features directly trace the excitation temperature of the gas. An estimation of the temperature of the H_2 could help constrain its location.

We created spectral templates of H_2 fluorescence with AU Mic's Lyα profile as we did in Section 3 using the models from McJunkin et al. (2016) with a uniform filling factor. Our grid of models covers from 300 to 3200 K in 100 K increments at column densities between $\log(N) = 15$ and $\log(N) = 20$ in increments of 0.2 dex. Because we are assuming the gas is thermally populated, we know the gas is at least 300 K and likely much warmer because of the ground-state energy levels of the FUV H_2 transitions. For each template, we calculated the likelihood, L, (Figure 8(a)) based on the CCF between the spectrum and each template as in Brogi & Line (2019) with

$$\ell = \log(L) = -\frac{N}{2}\log\left[s^2 - 2R + s_m^2\right] - N\log(2\pi), \quad (1)$$

where N is the number of points in the spectrum, s^2 is the variance in the spectrum, s_m^2 is the variance in the model, and R is the cross-covariance. The CCF height is equal to $\frac{R}{\sqrt{s_f^2 s_g^2}}$. We then translate that into confidence intervals based on the likelihood ratio test (Figure 9(a)). At these temperatures, the line ratios—all that the CCF is sensitive to—vary little, and the resulting uncertainties are large.

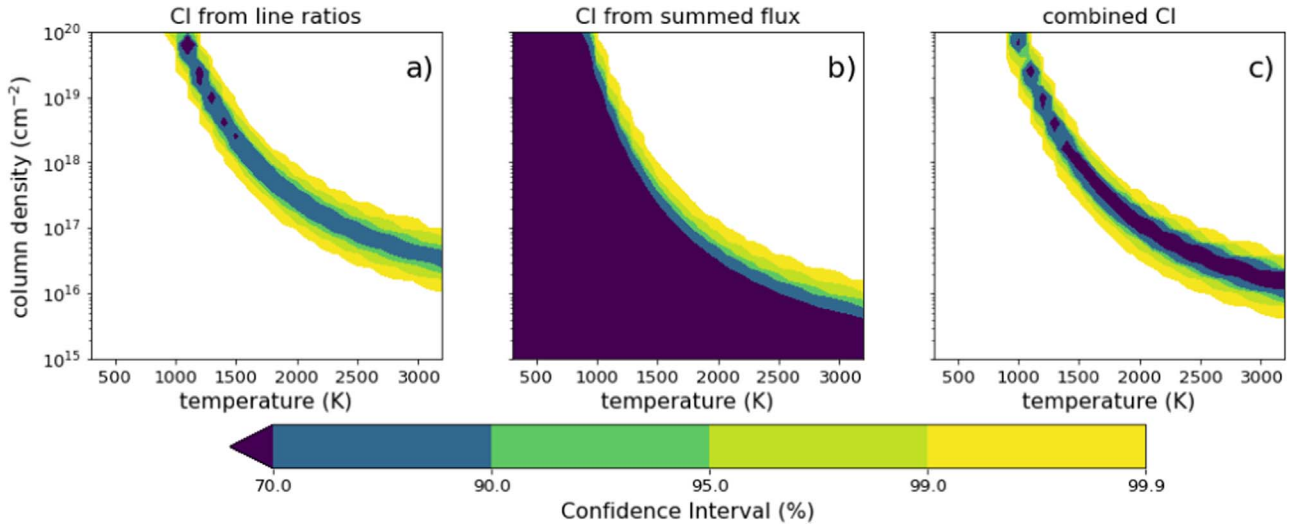

Figure 9. Confidence intervals for the temperature and H_2 column density of the gas.

To complement this analysis, we also measure the total H_2 emission in the spectrum to better constrain the H_2 temperature. We coadded the flux in the regions of the strongest H_2 lines to result in a coadded line profile, integrated the flux from that profile, and fit that integrated flux to what we obtained from the same procedure (coadding the strongest lines and integrating the flux of the resulting profile) for each model in the grid. While the coadded flux is more sensitive to different column densities and temperatures, there are also much larger uncertainties in calculating the coadded flux. For example, uncertainties in the Lyα reconstruction result in only a few percent uncertainties in the ratios of the amount of flux at the pumping wavelengths, but up to 30% uncertainties in the absolute flux. (Uncertainties in Lyα reconstruction are dominated by the column density of hydrogen in the ISM, which generally increases or decreases all the Lyα flux, thus having less effect on relative fluxes and more effect on absolute fluxes.) We also considered uncertainties from the continuum subtraction ($\sim 6.2 \times 10^{-16}$ erg s^{-1} cm^{-2}) and the flux uncertainties returned by the pipeline reduction ($\sim 3.8 \times 10^{-15}$ erg s^{-1} cm^{-2}). The final uncertainty in the flux measurement, σ, is the sum of all of these added in quadrature. The log-likelihood, ℓ is then calculated as

$$\ell = \log(L) = -\frac{1}{2}\left[\frac{(F_{\rm mod} - F_{\rm meas})^2}{\sigma^2} + \log(2\pi\sigma^2)\right], \quad (2)$$

where $F_{\rm meas}$ is the flux measured from coadding H_2 features in the data while $F_{\rm mod}$ is the flux from coadding the features in the model. This results in log likelihoods for our models as shown in Figure 8(b) with the corresponding confidence intervals in Figure 9(b).

Finally, we added the likelihoods from both the CCF and the coadded flux to produce the log likelihoods in Figure 8(c) and the confidence intervals in Figure 9(c). Our best-fit model has a log (N) = 17.6 and T = 1900 K, consistent with the temperature range from France et al. (2007) of 800 to 2000 K; our best column density estimate falls just outside the range from France et al. (2007) of 2.8×10^{15} to 1.9×10^{17} cm^{-2}. Our 95% confidence interval stretches beyond the limits of our grid, but we conclude the gas is at >1000 K with a 99.9% confidence. France et al. (2007) put an upper limit on the H_2 temperature based on the relative strength of O VI-pumped lines to Lyα-pumped lines: Only at temperatures below 2000 K do the O VI-pumped lines dominate in the way they do in the FUSE spectrum. Thus, we adopt a temperature range of 1000–2000 K for the H_2 during quiescence.

6. Discussion

We consider four different possible origins for the detected H_2 emission: an unrelated background/foreground source, the disk, the planet, or the star.

6.1. Unrelated Source

An unrelated source, such as a background object or interstellar gas, would not receive any detectable amount of heating from a flare. Thus, given that the H_2 flux increases as a response to the stellar flare, we can rule out a foreground or background source. Even without the flare, a background source is unlikely. Our detection is at the systemic radial velocity (RV) of the AU Mic system, so it would have to be a source not only at the same R.A. and decl., but also moving with the same velocity.

6.2. Disk

While other gas species have been detected in circumstellar disks as old as AU Mic, H_2 has not been confirmed in any disks older than 15 Myr (see review by Hughes et al. 2018). However, as mentioned in Section 1, H_2 is hard to detect due to its homonuclear nature, so this could merely be an observational bias. AU Mic is relatively nearby, which aids the ability to detect weak emission of H_2 in it.

6.2.1. Analysis Based on the LSD Profile

Line profiles from disks trace the location of the gas because the gas velocity approximately follows Kepler's laws, so the velocity decreases with increasing distance from the star. The average radius of the gas can be estimated by Equation (2) from Schindhelm et al. (2012):

$$r = GM_*\left(\frac{2sin(i)}{\rm FWHM}\right)^2, \quad (3)$$

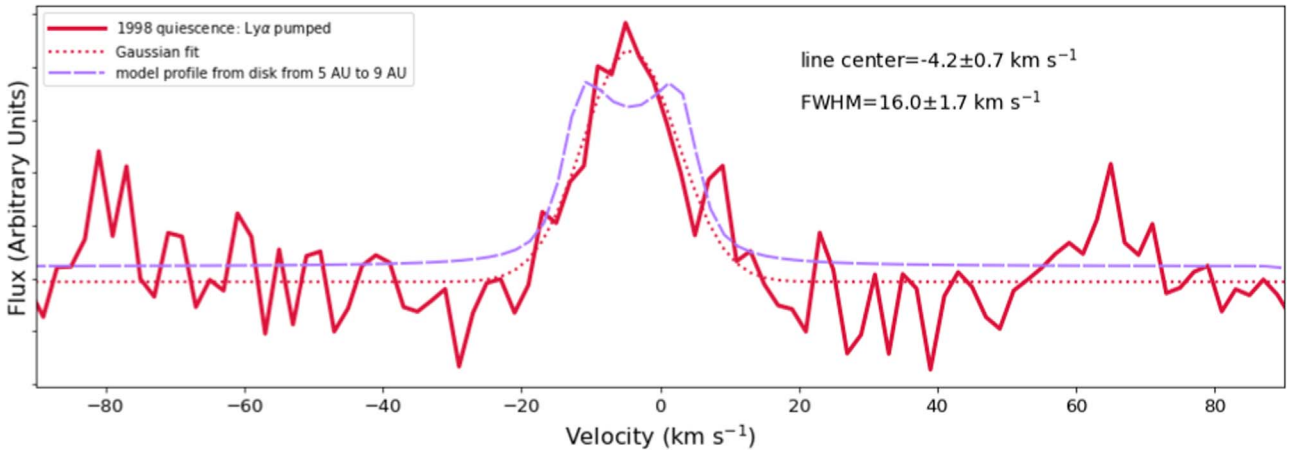

Figure 10. The line profile reconstructed using LSD compared with a model disk profile, assuming the gas was in a ring from 5 to 9 au.

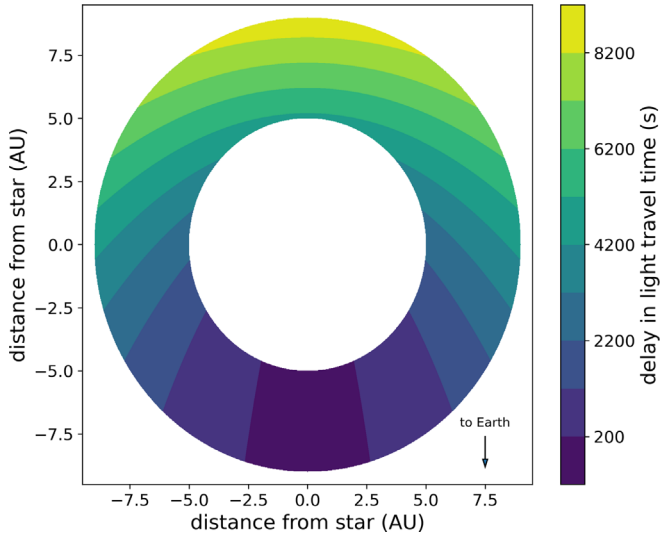

Figure 11. The delay in light-travel time, assuming the light went from the star to the spot in the disk before coming to us. Only parts of the disk in the darkest colored region, with delay times less than 200 s, are consistent with our measurements. If the emission can only come from the front part of the ring (to satisfy the time delay constraint), the line width of the line-of-sight emission would be smaller than the full velocity width of the ring.

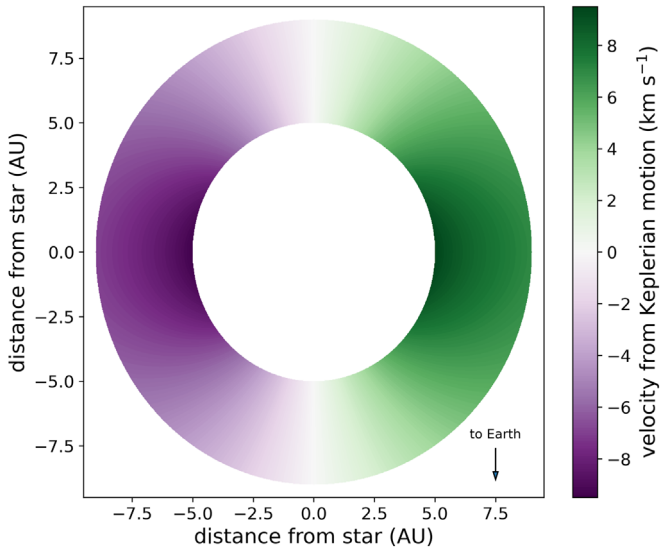

Figure 12. The Keplerian velocity—the dominant broadening component—of gas in a disk between 5 and 9 au, distances that would be consistent with the quiescent line profile. For an edge-on disk, the broadness of the line profile is the result of adding the emission from all parts of the disk.

where r is the distance of the gas from the star, M_* is the mass of the star, G is the gravitational constant, and i is the inclination of the disk. For AU Mic, the line profile from the H_2 during quiescence has an FWHM of 16.0 ± 1.7 km s^{-1}, as discussed in Section 3, which gives an average radius of ~7 au. This radius already poses problems, because given the flux from the star, heating the disk to $T > 1000$ K at 7 au is impossible based on our current understanding of disk physics.

We created a model profile based on this average radius, using a flat, optically thick disk model between 5 and 9 AU, assuming a stellar mass of 0.5 $M_\odot$ (Plavchan et al. 2020). Because we assume a flat disk, we also assume that the stellar flux absorbed—and thus the corresponding H_2 flux—scales as r^{-3}. This profile was then convolved with the line spread function (LSF) of the spectrograph. This modeled profile fits the LSD profile (Figure 10) reasonably well with regard to the width. However, the LSD profile lacks the characteristic "M" (double-peaked) shape profile from the line, which could indicate that the gas does not originate in the disk. While gas at larger radii could result in a more Gaussian-like profile, that would make heating the gas even more difficult than it is around 7 au.

The response to the flare makes a disk origin even less probable. The lines from [0,17] reach their peak in the flare up to 200 s after the C IV line flares (Figure 5). This rules out most locations in the disk, as light from the flare would not have enough time to travel from the star to most locations in the disk and then be reprocessed and redirected to us within 200 s. In Figure 11, we show the regions of the disk where it would be physically possible to detect light with at most a 200 s delay.

Additionally, the line profile from the flare is very similar to that during quiescence, with an FWHM of 19.0 ± 1.2 km s^{-1} during the flare compared to 16.6 ± 1.9 km s^{-1} in the 2020 quiescence observations. For disk emission lines, the width of the line profile is due to emission at different velocities in different parts of the disk (Figure 12). If the source of the H_2 was a disk, only a portion of the disk would be heated by the flare, and therefore, the line profile would be significantly narrower. Instead,

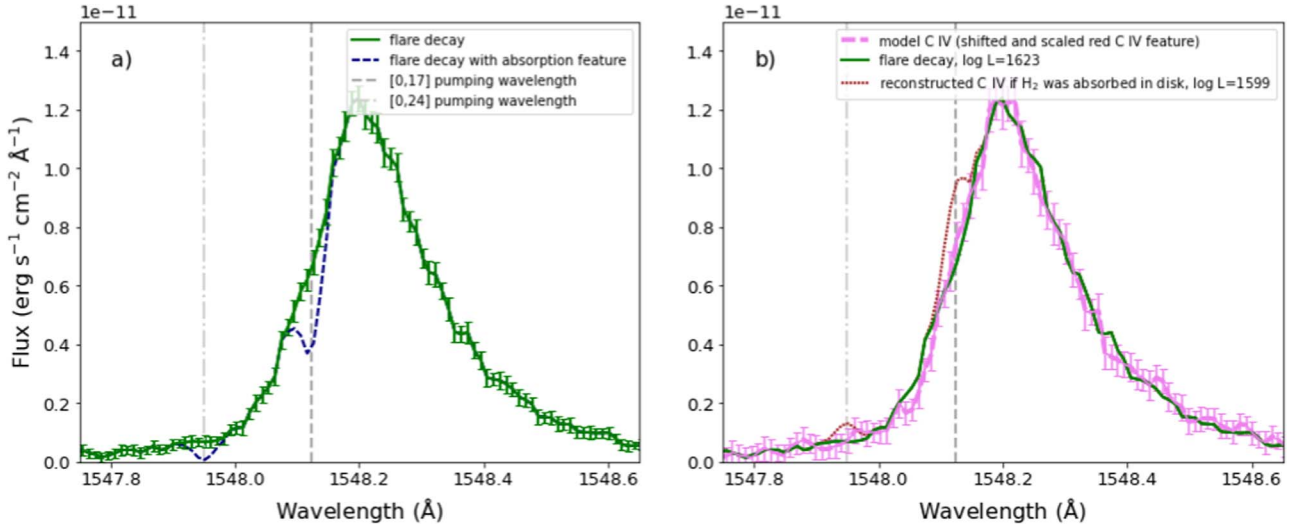

Figure 13. (Left) The observed C IV profile (solid green line) during the flare shows no absorption features at the pumping wavelengths, which are marked with vertical, dashed, gray lines, like we would expect (blue dashed line) if the H_2 was between the star and us. (Right) The observed flux matches better with the modeled C IV profile (thick pink dashed line) than the reconstructed C IV profile (brown dotted line) matches the modeled profile. The reconstructed profile is calculated by adding the potential absorption from the disk to the observed profile to recreate the intrinsic profile. Based on their corresponding likelihoods, the observed flux is a significantly better match for the modeled C IV profile, as the reconstructed C IV can be clearly ruled out, with a p-value of $<1 \times 10^{-10}$ in comparison to the observed flux being the intrinsic profile.

the line profile from the flare has a very similar width to that from quiescence, as shown in Figure 3.

6.2.2. Search for Absorption from the Disk in C IV

If the H_2 that is being pumped by C IV during the flare is at a few astronomical units, we should be able to detect absorption in C IV if the gas is between us and the flare. The scale height, h, of gas in a disk is approximately

$$h = c_s \sqrt{\frac{2r^3}{GM_*}}, \tag{4}$$

where c_s is the sound speed (Hartmann 2008). Given a gas temperature, T, of 1500 K, and assuming all the gas is in H_2, so that the mean molecular weight μ is 2.016,[12] we can calculate the sound speed using $c_s = \sqrt{\frac{k_B T}{\mu m_H}} = 2.3 \text{ km s}^{-1}$, where k_B is Boltzmann's constant and m_H is the mass of hydrogen. At even 3 au, Equation (4) gives a scale height of $\sim$175 $R_\odot$, increasing to $\sim$375 $R_\odot$ at 5 au. Given that the disk is almost edge on, with an inclination of at least 88° (Daley et al. 2019), the disk need only have a scale height of 22 $R_\odot$ at 3 au or 38 $R_\odot$ at 5 au to obscure the star, far less than the scale heights we calculate.

We modeled the absorption we would expect to see from the disk at the pumping wavelengths with a Gaussian. The total flux absorbed out of the C IV line is measured using the observed fluxes in the pumped lines and their respective branching ratios. When estimating the flux absorbed out of the C IV line in this way, we add back the predicted flux to the pumping transition itself as the branching ratios predict that some fraction of the absorbed flux will be re-emitted at this same wavelength. Thus, we estimate the actual absorption that would be seen on Earth. For [0,17] we used the average absorbed flux based on the six strongest features; for [0,24] we took the average of both detected features. The widths of the absorption features are those from thermal broadening at 1500 K plus the additional width from the line spread function added in quadrature, while the total flux is the one calculated as described above. We then subtracted this absorption feature from the observed flux (Figure 13(a), solid green line) to see if such absorption would be detectable—and it clearly is, as shown by the blue dashed line in the plot. This calculation assumes the gas is distributed spherically; if the gas were in a column or a flat disk, the predicted absorption would be deeper.

Furthermore, if the observed flux was the result of H_2 absorption, then adding that emission back should result in the intrinsic C IV profile. We modeled the true C IV profile (the dashed pink line in Figure 13(b)) by using the observed flux from the red component of the C IV emission, centered at 1550.94 Å. We Doppler-shifted that observed red C IV profile and scaled it by a constant to match the blue component, creating a "modeled" C IV profile. The observed flux is a very good match for our modeled C IV, while the reconstructed C IV profile (the brown dotted line, calculated by adding the potential absorption from the disk to the observed profile to recreate the corresponding intrinsic profile) is a poor match. We also calculated the likelihood for both the reconstructed C IV profile and the observed C IV profile in a similar manner to that of Equation (2):

$$\log(L) = -\frac{1}{2}\sum_i \left[\frac{(F_{\text{mod},i} - F_{\text{meas},i})^2}{\sigma_i^2} + \log(2\pi\sigma_i^2) \right], \tag{5}$$

where in this case the "measured" flux, $F_{\text{meas},\,i}$, is the flux at each point of the shifted and scaled C IV profile that we assume to be the shape of the intrinsic profile, while the modeled flux is either the observed C IV profile flux or the reconstructed C IV profile. Based on their corresponding likelihoods, the observed flux is a significantly better match for the intrinsic C IV profile, as the reconstructed C IV can be clearly ruled out, with a p-value of $<1 \times 10^{-10}$ in comparison to the observed flux being the intrinsic profile. Thus, we conclude that the absorption in

[12] https://pubchem.ncbi.nlm.nih.gov/compound/Hydrogen

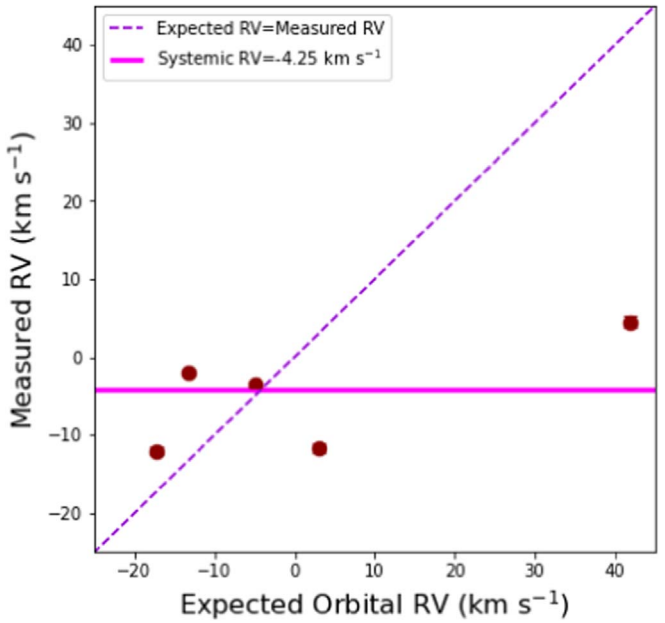

Figure 14. The velocities we measured from 2020 vs. what we would expect if the H_2 was in AU Mic b based on the orbit from Plavchan et al. (2020). We do not see the signal follow the planet's orbit—instead, it scatters around the systemic velocity of the star. Uncertainties are plotted but are generally smaller than the marker.

the C IV profile at the pumping wavelengths that we would expect to see if the H_2 were between us and the C IV is not present. Either the scale height we calculated is too large by an order of magnitude or the H_2 is not in the disk.

6.3. A Planet

While H_2 has not been conclusively detected in an exoplanet (e.g., France et al. 2010; Kruczek et al. 2017), all models indicate that it should be prominent in gas-giant exoplanets, similar to the gas-giant planets in our solar system (e.g., Sudarsky et al. 2003; Yelle 2004). This is especially true for young planets that have not yet undergone significant atmospheric escape. Because the effective temperatures of the planets orbiting AU Mic have not been measured, we cannot rule either planet out as a source of the H_2 based on their temperature.

However, in the 2020 observations, which span 23 hr (after discarding the observation with the flare), AU Mic b's projected velocity changes from -17 to 42 km s^{-1} based on the orbital parameters from Martioli et al. (2021). This is not reflected in the CCF. In Figure 14, we plot the measured CCF velocity centers as a function of time, compared with the predicted velocity of the planet. The velocities of the CCF are consistent with the systemic velocity—which would be the expected central velocity for both the star and the disk—but not AU Mic b's velocity. AU Mic c can be ruled out for the same reason, as its expected velocities during these observations are all more than 30 km s^{-1} from the systemic velocity. Thus, the H_2 line emission is not from either Au Mic b or c.

6.4. The Star

By process of elimination, the most likely source for the observed H_2 is the star, consistent with the inferred location of H_2 in older M dwarfs (Kruczek et al. 2017). To check whether the star is a possible source, we fit the LSD line profile from Figure 2 with a simple model of an emission line arising on the stellar surface that includes thermal broadening, rotational broadening, and instrumental broadening. Our best fit from using a Markov Chain Monte Carlo (MCMC) algorithm is shown in Figure 15. The best-fit parameters, along with their corresponding priors, are summarized in Table 5; the full distribution from the MCMC for each parameter is shown in Figure 16. Based on this simulation, we estimate $9.91^{+1.64}_{-1.54}$ km s^{-1} for the $v \sin i$, which is consistent with the 8.7 ± 2.0 km s^{-1} (Table 1) found by Plavchan et al. (2020) using photospheric lines.

The profile during the flare is slightly broader and more blueshifted than the quiescent profile (Figure 3, Table 3). We attribute this to the possible detection of mass motion of H_2 during the flare, similar to mass motion detected during solar flares (e.g., Ohyama & Shibata 1997), as we cannot produce such a profile with the expected emission from H_2.

Based on expected temperatures, H_2 can exist in both the photospheres and starspots of M dwarfs. AU Mic is not the only star with this cold H_2. France et al. (2020) detected cold H_2 (which also brightened during a flare) in Barnard's Star, a $\sim$10 Gyr M3.5 dwarf. Given its age, Barnard's Star is very unlikely to have detectable quantities of residual circumstellar gas; thus, the H_2 must originate from the star itself.

However, the measured temperature of the H_2 (<2000 K) is inconsistent with that of AU Mic's photosphere ($T_{\rm eff} = 3642 \pm 22$ K; Pecaut & Mamajek 2013). So where in the star is it coming from? We consider two possibilities: starspots and the temperature minimum in a cold layer between the photosphere and the chromosphere.

There are two main ways to estimate the starspot temperatures for AU Mic: by models or by observations. There have been models of starspot temperatures for main-sequence M0 dwarfs, which estimate temperatures of 3000 K (Panja et al. 2020). However, because AU Mic is more active than typical main-sequence stars, with a radius that is 50% larger than it will have once it reaches the main sequence (Baraffe et al. 2015), it is possible that these differences would also cause a change in starspot temperatures. From an observational perspective, starspot temperatures measured specifically for AU Mic by using photometric (Rodono et al. 1986) or spectroscopic (Afram & Berdyugina 2019)) data are far warmer than the H_2 temperature we measure, as are starspot temperature measurements for other young dwarfs (Gully-Santiago et al. 2017). However, there is indirect evidence that starspots could be colder than these estimates. In the Sun, which has a $T_{\rm eff}$ 2000 K warmer than AU Mic's, molecules in the sunspots have rotational and vibrational temperatures less than 2000 K (e.g., Mulchaey 1989; Sriramachandran & Shanmugavel 2011), indicating starspots might also get cooler than models predict. Furthermore, starspots need not all be the same temperature (e.g., Kopp & Rabin 1992). If some starspots are at temperatures corresponding to the ones measured by Afram & Berdyugina (2019), we do not think this completely excludes the possibility of colder starspots. Plus, like the photosphere, an individual starspot has layers of different temperatures. Therefore, we cannot rule out starspots across the star as a potential source of the H_2.

The other possibility is a layer of colder gas at the top of the photosphere near the temperature minimum. In the Sun, this layer is called the CO-mosphere (Ayres 2002), because it is cool enough ($T \sim 3500$ K) for CO to form compared to the

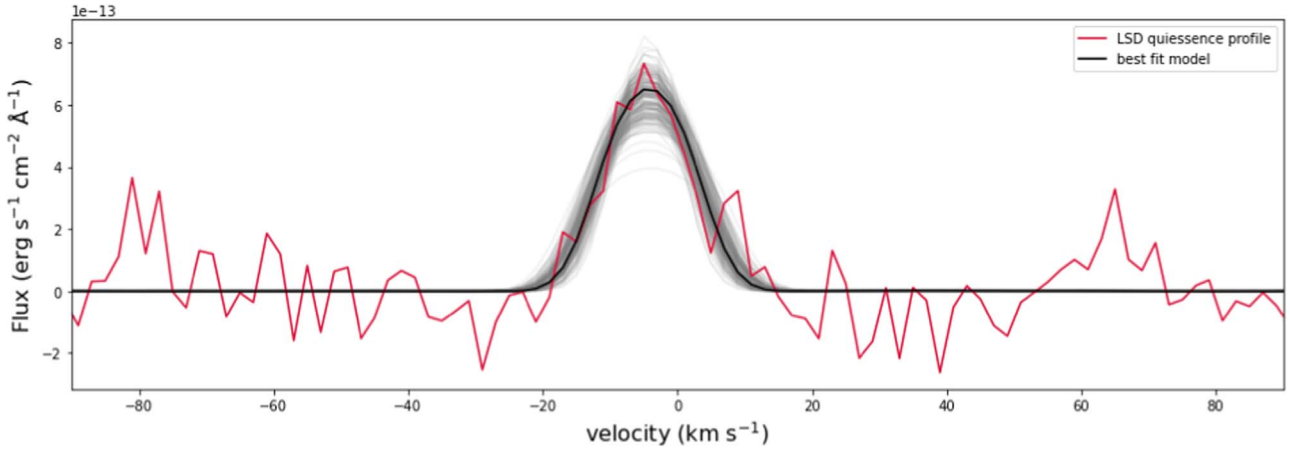

Figure 15. The LSD profile plotted with the best fit from our MCMC simulation. Also plotted are 200 samples to show the distribution of potential solutions.

Table 5
Model Parameters

Parameter	Best-fit Value	Priors
RV (km s^{-1})	-4.25 ± 0.23	$\mathcal{N}(-4.25,0.24)$
$v \sin i$ (km s^{-1})	$9.91^{+1.64}_{-1.54}$	$\mathcal{U}(2,22)$
T_{ex} (K)	1528^{+329}_{-356}	$\mathcal{U}(1000,2000)$

Note. 1σ uncertainties are calculated based on the values at the 16th and 84th percentiles, as shown in Figure 16.

Sun's effective temperature of 5800 K (Noyes & Hall 1972; Ayres & Testerman 1981; Wiedemann et al. 1994). In the case of AU Mic, the photosphere is cold enough for CO to form anywhere, so the name of the layer would be different, but the basic structure of a colder layer could easily hold. Cold layers occur in M giants, producing H_2O that cannot exist in those stars' deeper photospheres (Sloan et al. 2015), but similar structures have not been detected in M dwarfs. Current models indicate that there should be a cold layer between the photosphere and the chromosphere, but again, the modeled gas does not get cold enough, as it is predicted to only reach ~2500 K (Fontenla et al. 2016). Still, as the physics of the temperature structure in the top of the photosphere for M dwarfs is undoubtedly complicated and has not been extensively studied, we think it is possible that current models do not capture all the physics of such star's atmospheric structure.

There is a third possibility. Our temperature calculations assume that H_2 is populated thermally because models of disk heating are consistent with thermal heating (Ádámkovics et al. 2016). While there is no evidence of this, we cannot rule out some degree of the nonthermal population that would skew our temperature measurement. However, in the case of Jupiter, temperature estimates from line ratios are warmer than the kinetic temperature estimates (Barthélemy et al. 2005). Jupiter is obviously much colder than the temperatures we measured, but if the same holds true for AU Mic, the temperature of the H_2 is even less than our 1000–2000 K estimate and would not explain the temperature discrepancy.

7. Conclusions

In this paper, we report on our analysis of H_2 in AU Mic including

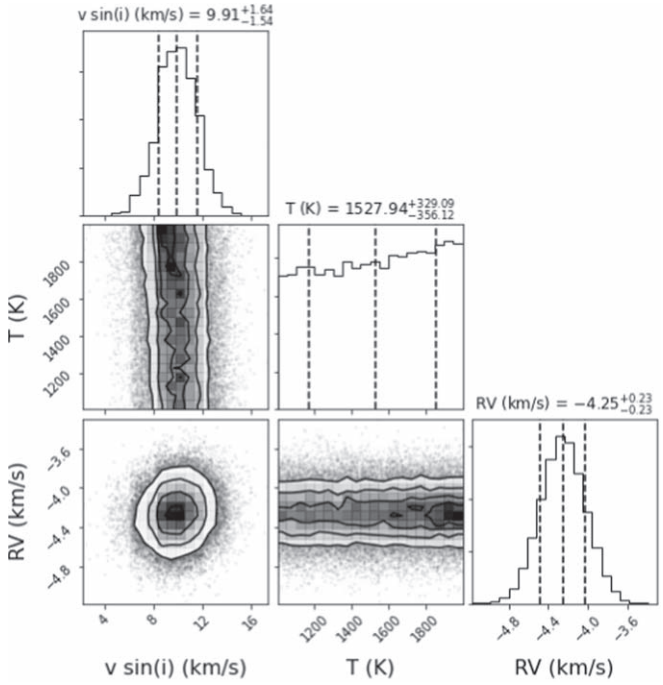

Figure 16. Resulting distributions from the MCMC simulation. The median value is marked, as are the 16th and 84th percentiles, representing the 1σ uncertainties. Our value for $v \sin i$ is consistent with that measured from photospheric lines (Plavchan et al. 2020).

1. detecting H_2 in AU Mic from HST-STIS FUV spectra both during quiescence and a flare,
2. measuring the temperature of the H_2 during quiescence at >1000 K,
3. characterizing the response of the H_2 to a stellar flare, showing nonthermal emission pumped by C IV,
4. ruling out a foreground/background source, the circumstellar disk, or a planet as the source of this H_2.

Based on the line profile and the response to a stellar flare, we conclude that the only possible source of the H_2 is in the star itself. However, the temperatures we measure indicate that this gas is too cold to be from the star based on current models of M dwarfs and their spots.

This detection obviously presents a mystery. Current models cannot account for this H_2—but it seems clear that the H_2 emission must be produced by the star.

Based on observations with the NASA/ESA Hubble Space Telescope obtained at the Space Telescope Science Institute, which is operated by the Association of Universities for Research in Astronomy, Incorporated, under NASA contract NAS5-26555. Support for program number (GO-15310) was provided through a grant from the STScI under NASA contract NAS5-26555. G.J.H. is supported by by general grant 12173003 awarded by the National Science Foundation of China. This research has made use of the VizieR catalog access tool, CDS, Strasbourg, France. The original description of the VizieR service was published by Wenger et al. (2000). This research has made use of the SIMBAD database, operated at CDS, Strasbourg, France.

Facility: HST (STIS).

Software: SpecTres (Carnall 2017), NumPy (Oliphant 2006; Van Der Walt et al. 2011), Pandas (pandas development team 2020), Matplotlib (Hunter 2007), LMFIT (Newville et al. 2014), emcee (Foreman-Mackey et al. 2013).

Appendix
Individual H_2 Features from the 2020 Flare

The H_2 features detectable by eye during the 2020 flare are from the [0,17] (Figure A1) and [0,24] (Figure A2) progressions.

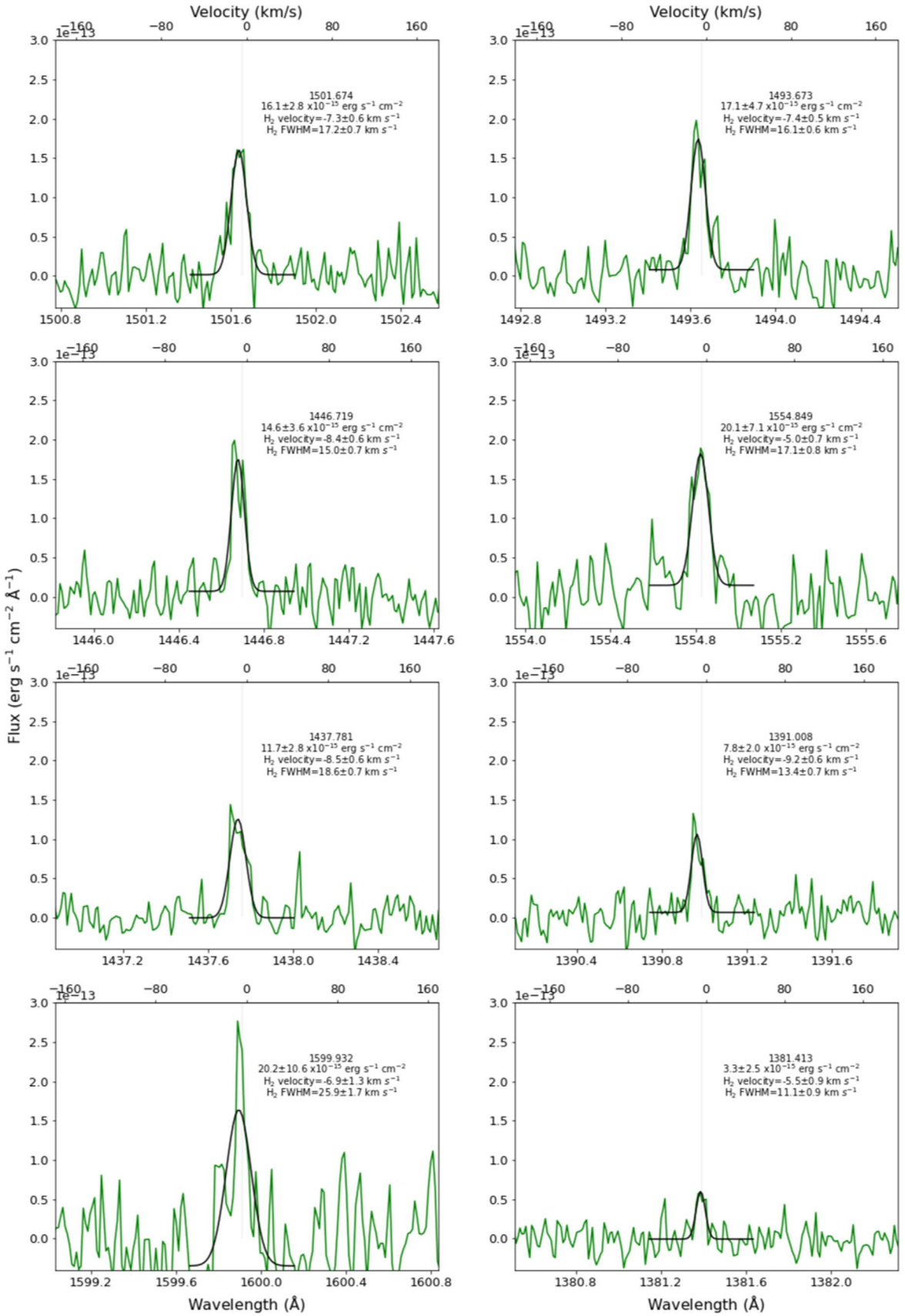

Figure A1. Gaussian fits to H_2 profiles for features in the [0,17] progression from observation OE4H01010 acquired on 2020 July 2.

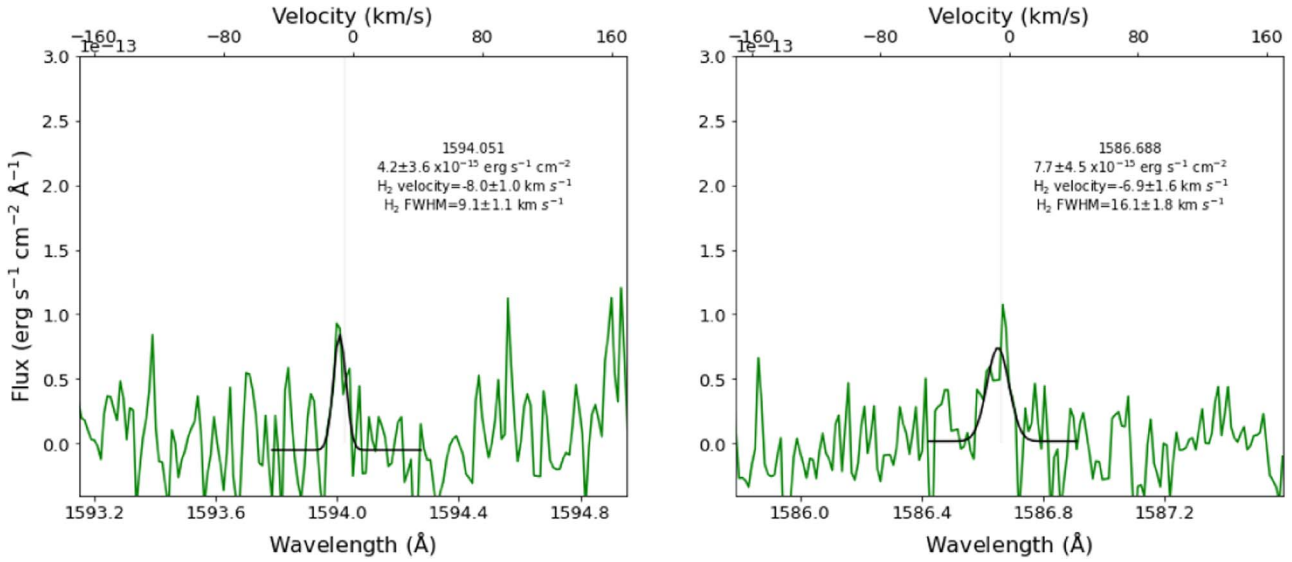

Figure A2. Gaussian fits to H_2 profiles for features in the [0,24] progression from observation OE4H01010 acquired on 2020 July 2.

ORCID iDs

Laura Flagg https://orcid.org/0000-0001-6362-0571
Christopher M. Johns-Krull https://orcid.org/0000-0002-8828-6386
Kevin France https://orcid.org/0000-0002-1002-3674
Gregory Herczeg https://orcid.org/0000-0002-7154-6065
Allison Youngblood https://orcid.org/0000-0002-1176-3391
Adolfo Carvalho https://orcid.org/0000-0002-9540-853X
John Carptenter https://orcid.org/0000-0003-2251-0602
Scott J. Kenyon https://orcid.org/0000-0003-0214-609X
Elisabeth Newton https://orcid.org/0000-0003-4150-841X
Keighley Rockcliffe https://orcid.org/0000-0003-1337-723X

References

Abgrall, H., Roueff, E., Launay, F., Roncin, J. Y., & Subtil, J. L. 1993, A&AS, 101, 273
Ádámkovics, M., Najita, J. R., & Glassgold, A. E. 2016, ApJ, 817, 82
Afram, N., & Berdyugina, S. V. 2019, A&A, 629, A83
Alcalá, J. M., Manara, C. F., France, K., et al. 2019, A&A, 629, A108
Ayres, T. R. 2002, ApJ, 575, 1104
Ayres, T. R., & Testerman, L. 1981, ApJ, 245, 1124
Baraffe, I., Homeier, D., Allard, F., & Chabrier, G. 2015, A&A, 577, A42
Barrado y Navascués, D., Stauffer, J. R., Song, I., & Caillault, J.-P. 1999, ApJL, 520, L123
Barthélemy, M., Lilensten, J., & Parkinson, C. 2005, A&A, 437, 329
Baruteau, C., Crida, A., Paardekooper, S.-J., et al. 2014, in Protostars and Planets VI, ed. H. Beuther (Tucson, AZ: Univ. Arizona Press), 667
Brogi, M., & Line, M. R. 2019, AJ, 157, 114
Carlberg, J. K., & Monroe, T. 2017, Instrument Science Report STIS, 2017-6
Carnall, A. C. 2017, arXiv:1705.05165
Chen, W., & Johns-Krull, C. M. 2013, ApJ, 776, 113
Daley, C., Hughes, A. M., Carter, E. S., et al. 2019, ApJ, 875, 87
Donati, J.-F., Semel, M., Carter, B. D., Rees, D. E., & Collier Cameron, A. 1997, MNRAS, 291, 658
Flagg, L., Johns-Krull, C. M., France, K., et al. 2021, ApJ, 921, 86
Fontenla, J. M., Linsky, J. L., Witbrod, J., et al. 2016, ApJ, 830, 154
Foreman-Mackey, D., Hogg, D. W., Lang, D., & Goodman, J. 2013, PASP, 125, 306
France, K., Roberge, A., Lupu, R. E., Redfield, S., & Feldman, P. D. 2007, ApJ, 668, 1174
France, K., Stocke, J. T., Yang, H., et al. 2010, ApJ, 712, 1277
France, K., Duvvuri, G., Egan, H., et al. 2020, AJ, 160, 237
Goldreich, P., & Sari, R. 2003, ApJ, 585, 1024
Graham, J. R., Kalas, P. G., & Matthews, B. C. 2007, ApJ, 654, 595
Gully-Santiago, M. A., Herczeg, G. J., Czekala, I., et al. 2017, ApJ, 836, 200
Hartmann, L. 2008, Accretion Processes in Star Formation (Cambridge: Cambridge Univ. Press)
Herczeg, G. J., Linsky, J. L., Walter, F. M., Gahm, G. F., & Johns-Krull, C. M. 2006, ApJS, 165, 256
Hughes, A. M., Duchêne, G., & Matthews, B. C. 2018, ARA&A, 56, 541
Hunter, J. D. 2007, CSE, 9, 90
Ingleby, L., Calvet, N., Bergin, E., et al. 2009, ApJL, 703, L137
Jordan, C., Brueckner, G. E., Bartoe, J.-D. F., Sandlin, G. D., & Vanhoosier, M. E. 1978, ApJ, 226, 687
Kalas, P., Liu, M. C., & Matthews, B. C. 2004, Sci, 303, 1990
Kenyon, S. J., Najita, J. R., & Bromley, B. C. 2016, ApJ, 831, 8
Kopp, G., & Rabin, D. 1992, SoPh, 141, 253
Krist, J. E., Ardila, D. R., Golimowski, D. A., et al. 2005, AJ, 129, 1008
Kruczek, N., France, K., Evonosky, W., et al. 2017, ApJ, 845, 3
Kunkel, W. E. 1970, PASP, 82, 1341
Liu, M. C., Matthews, B. C., Williams, J. P., & Kalas, P. G. 2004, ApJ, 608, 526
Loyd, R. O. P., France, K., Youngblood, A., et al. 2018, ApJ, 867, 71
Lyra, W., & Kuchner, M. 2013, Natur, 499, 184
MacGregor, A. M., Osten, R. A., & Hughes, A. M. 2020, ApJ, 891, 80
MacGregor, M. A., Wilner, D. J., Rosenfeld, K. A., et al. 2013, ApJL, 762, L21
Mamajek, E. E., & Bell, C. P. M. 2014, MNRAS, 445, 2169
Martioli, E., Hébrard, G., Correia, A. C. M., et al. 2021, A&A, 649, A177
Matthews, B. C., Kennedy, G., Sibthorpe, B., et al. 2015, ApJ, 811, 100
McJunkin, M., France, K., Schindhelm, E., et al. 2016, ApJ, 828, 69
Monsignori Fossi, B. C., Landini, M., Del Zanna, G., & Bowyer, S. 1996, ApJ, 466, 427
Mulchaey, J. S. 1989, PASP, 101, 211
Newville, M., Stensitzki, T., Allen, D. B., & Ingargiola, A. 2014, LMFIT v0.8.8, Zenodo doi: 10.5281/zenodo.11813
Noyes, R. W., & Hall, D. N. B. 1972, BAAS, 4, 389
Ohyama, M., & Shibata, K. 1997, PASJ, 49, 249
Oliphant, T. E. 2006, A Guide to NumPy (USA: Trelgol Publishing), http://www.numpy.org/
Pagano, I., Linsky, J. L., Carkner, L., et al. 2000, ApJ, 532, 497
pandas development team 2020, Pandas v1.4.3, Zenodo, doi:10.5281/zenodo.6702671
Panja, M., Cameron, R., & Solanki, S. K. 2020, ApJ, 893, 113
Pecaut, M. J., & Mamajek, E. E. 2013, ApJS, 208, 9
Plavchan, P., Barclay, T., Gagné, J., et al. 2020, Natur, 582, 497
Roberge, A., Weinberger, A. J., Redfield, S., & Feldman, P. D. 2005, ApJL, 626, L105
Robinson, R. D., Linsky, J. L., Woodgate, B. E., & Timothy, J. G. 2001, ApJ, 554, 368
Rodono, M., Cutispoto, G., Pazzani, V., et al. 1986, A&A, 165, 135
Schindhelm, E., France, K., Burgh, E. B., et al. 2012, ApJ, 746, 97
Schneider, A. C., Shkolnik, E. L., Allers, K. N., et al. 2019, AJ, 157, 234
Schneider, P. C., & Schmitt, J. H. M. M. 2010, A&A, 516, A8

Shkolnik, E. L., Allers, K. N., Kraus, A. L., Liu, M. C., & Flagg, L. 2017, AJ, 154, 69
Sloan, G. C., Goes, C., Ramirez, R. M., Kraemer, K. E., & Engelke, C. W. 2015, ApJ, 811, 45
Smith, K., Güdel, M., & Audard, M. 2005, A&A, 436, 241
Sriramachandran, P., & Shanmugavel, R. 2011, Ap&SS, 336, 379
Sudarsky, D., Burrows, A., & Hubeny, I. 2003, ApJ, 588, 1121
Van Der Walt, S., Colbert, S. C., & Varoquaux, G. 2011, CSE, 13, 22
Wang, J. J., Graham, J. R., Pueyo, L., et al. 2015, ApJL, 811, L19
Weidenschilling, S. J. 1977, MNRAS, 180, 57
Wenger, M., Ochsenbein, F., Egret, D., et al. 2000, A&AS, 143, 9
Wiedemann, G., Ayres, T. R., Jennings, D. E., & Saar, S. H. 1994, ApJ, 423, 806
Wilner, D. J., Andrews, S. M., MacGregor, M. A., & Hughes, A. M. 2012, ApJL, 749, L27
Yang, H., Herczeg, G. J., Linsky, J. L., et al. 2012, ApJ, 744, 121
Yelle, R. V. 2004, Icar, 170, 167
Youdin, A. N., & Goodman, J. 2005, ApJ, 620, 459
Youngblood, A., Pineda, J. S., & France, K. 2021, ApJ, 911, 112
Youngblood, A., France, K., Loyd, R. O. P., et al. 2016, ApJ, 824, 101